
Role of the dipole jet in inclined stroke plane kinematics of insect flight

S.Deepthi¹, S.Vengadesan^{1 2*}

1 Department of Applied Mechanics, Indian Institute of Technology Madras, Chennai, Tamil Nadu, India

2 Adjunct Faculty, Department of Mechanical Engineering, Virginia Tech, Blacksburg, VA, USA

Abstract

The two-dimensional (2D) inclined stroke plane kinematics of insect wing is studied for various stroke plane angles using the Immersed Boundary (IB) solver. The numerical results revealed the dominant lift enhancement mechanisms for this class of flows. The generated dipole was analysed to find the maximum velocity, inclination and spread. The analysis of these dipole characteristics for the different stroke plane angles exposed the alternate method to study the vertical force variation with the stroke plane angles. Lift enhancement mechanisms and dipole characteristics complement the high vertical force coefficient for the stroke plane angle of 60° commonly used by dragonflies during hover. The location of the dipole for different stroke plane angles identified a region of influence around the wing and demonstrated the role of the dipole jet in multi-body dynamics and wall effects.

Keywords: insect flight, aerodynamics, inclined stroke plane, dipole jet, flapping wing

1 Introduction

The design of biomimetic Micro Aerial Vehicle (MAV) requires a thorough understanding of insect flight. Flying insects with their agility and high-frequency flapping flight make them the most suitable for the study of flight characteristics. Especially, dragonfly with its two pairs of wings which are independently controlled is of great significance. Unlike the fruit flies which employ the horizontal stroke plane motions, the dragonfly employs the inclined motion producing significantly more lift.

The Biomimetic MAVs typically operate at the Reynolds number of 100. Under these conditions, viscous forces dominate the flow. At high reduced frequency and a high wing beat amplitude (i.e.) during hover, the flow becomes highly unsteady. The quasi-steady model^[1] suggested in the pioneering work, under-predicts the aerodynamic forces. Unsteady phenomena of delayed stall, rotational lift, added mass and wake capture were shown to describe the high lift. A comprehensive review of the unsteady aerodynamics was done in several review papers^[2,3]. The delayed stall^[4] is caused, when a large suction force is produced on the upper surface of the due to the presence of Leading Edge Vortex

(LEV). The presence of LEV during the acceleration phase gives a lift enhancement. Similarly, when the previously shed vortex pair causes induced velocity on the wing and alters the force generation, it is called the wake capture^[5]. Wake capture was later reported^[6] to both increase and decrease lift. Velocity induced perpendicular to the movement of the foil increases the lift forces on the foil, whereas velocity parallel to it reduces the lift due to the low-pressure region underneath it. Furthermore, rotational forces^[7] are caused, when the large vorticity generated during rotation (supination or pronation) adds to the circulation producing more lift. When the accelerated fluid exerts a pressure on the wing during stroke reversal, it is termed as Added Mass^[8]. These mechanisms could essentially describe most of the lift enhancement during flapping.

With the developments in Computational Fluid Dynamics (CFD), the instantaneous forces are predicted by the unsteady numerical simulations. Numerical simulation on a simple 2D inclined stroke plane kinematics was shown to balance the weight of the insect^[9]. A number of numerical simulations and experiments were conducted on a 2D wing by changing the kinematics^[8,10–12] and the Reynolds number^[9,10,13], revealed vortex dynamics relevant to insect flight. They uncovered the underlying physics and are of great interest in the design of MAVs. The experiment^[14] showed that span-wise flow that occurs on the 3D wing stabilised the LEV. Nevertheless, the 2D insect kinematics could represent the 3D flow behaviour around the flapping wing adequately at low Reynolds numbers^[15].

Moreover, the effect of external factors such as ground^[16–19] and gust^[20,21] was shown to influence the force generation significantly. Additionally, numerical simulations of tandem wings^[22–24] demonstrated that aerodynamic characteristics of the wing could be considerably changed for each phase of flight, with different phase angle and kinematics.

Horizontal stroke plane kinematics, commonly known as ‘Normal Hovering’ is used by most insect classes, with the exception of the Papilionidea, Syrphinae and Odonata^[25], where inclined stroke plane

kinematics is used. During hover, stroke plane angles of 0° and 60° are most widely studied in literature. Insects are seen to deviate from these typical values within 10° to 15° ^[26]. They maintain the same wing inclination angle with the horizontal plane, by varying their body angle. Nevertheless, the need for changing the stroke plane angle and its effect on force generation is most significant and valuable.

Interestingly, Wang^[27] studied a family of inclined kinematics by varying the mean angle of attack and the stroke plane angle such that it produces a resultant vertical force (upward). It showed that the stroke plane angle of 60° used by dragonflies is a cut-off for vertical force and emphasized the need for investigating it further. In addition, a vertically downward jet of the dipole was shown to increase with stroke plane angles. Further, Trizila^[28] reported about a downward jet region of the vortex street (fluid entrainment) caused an asymmetry and reduced lift during the horizontal flapping of 2D and 3D wings.

The literature review has brought the necessity for studying the influence of the stroke plane angle on force generation and vortex dynamics. In addition, it showed that studies on dipole jet could lead to interesting impacts on the aerodynamics of insect flight, which is often neglected in previous studies. In our current study, we systematically investigate the effect of stroke plane angles and study the vortex dynamics. We define and quantify the dipole jet to understand its effect on the forces.

2 Numerical method

The Immersed Boundary solver in foam–extend 4.0^{[29][30]}, a opensource CFD toolbox which is fork of OpenFOAM^[31] is used for the study. While using the conventional conformal mesh, the high angle of rotation and translation associated with flapping flight causes the mesh to become skewed reducing its quality. Immersed Boundary Method (IBM)^[32] which uses a stationary Cartesian mesh in the background with Lagrangian points to model the geometry, is preferred. A particular method of IBM, i.e. discrete direct imposition of boundary condition is used, which is summarised in the report^[33] along with its pros and cons.

$$\nabla \cdot \mathbf{u} = 0 \quad (1)$$

$$\frac{\partial \mathbf{u}}{\partial t} + \mathbf{u} \cdot \nabla \mathbf{u} = -\frac{\nabla p}{\rho} + \nu \Delta \mathbf{u} \quad (2)$$

The solver IcoDyMibFoam is used for the study. In this solver, the continuity and incompressible Navier-Stokes equation (Eq. (1) and (2)) are solved using PISO algorithm (Pressure-Implicit with Splitting of Operators). In the equations, \mathbf{u} is the fluid velocity, p fluid pressure, ρ density and ν kinematic viscosity. The sharp implementation of IB causes spurious oscillation^[34] in the velocity and pressure, when fluid regime changes to solid and vice versa, for moving bodies. This is overcome by taking moving averages of the force data. A few benchmark cases of the solver has been reported^[34].

3 Problem definition and validation

3.1 Problem definition

In the present work, the stroke plane inclination is varied to understand its effect on the vortex dynamics and dipole jet. The generalized two-dimensional inclined stroke plane kinematics proposed by Wang^[9] is used for the study. More details can also be found in Xu and Wang^[35]. Cross-section of the wing is modelled using an ellipse of aspect ratio 0.25. The position vector is taken at the centre of the

elliptical wing of chord C and is given by Eq. (3). It's rotation with respect to the horizontal plane is given by Eq. (4).

$$[x(t), y(t)] = \frac{A_0}{2C} \cos(2\pi f) (\cos \beta, \sin \beta) \quad (3)$$

$$\alpha(t) = \alpha_0 \sin(2\pi f) \quad (4)$$

A_0 and α_0 are amplitudes of translation and rotation respectively. β is the stroke plane angle, also called the angle of inclination and f is the frequency of oscillation. The maximum translational velocity is given by $U = \pi f A_0$ and time period is given by $T_f = 1/f$. The time scale used for validation study is $t_f = CT_f/\pi A_0$. The simulations are carried out at $Re = 157$, $A_0/C = 2.5$, $A_0 = 45^\circ$, $\alpha_0 = 45^\circ$, $\beta = 30^\circ, 45^\circ, 60^\circ, 75^\circ$.

$$C_V = F_V/0.5\rho U^2C \quad (5)$$

$$C_H = F_H/0.5\rho U^2C \quad (6)$$

The force coefficients C_V and C_H are obtained using Eq. (5) and (6) from the vertical (F_V) and horizontal forces (F_H). The computational domain for the proposed set of cases and its boundary conditions are given in Fig. 1. When the insect is hovering, boundaries are given zero velocity gradients and a zero relative pressure. The validations are given in the following sections.

3.2 Dragonfly kinematics

The code is validated for the solver settings against various standard benchmark cases such as stationary cylinder, linearly oscillating cylinder and transversely oscillating cylinder with inflow and dragonfly kinematics in hover. The results of the hovering flight of dragonfly i.e., the kinematics described in section 3.1 with $\beta=60^\circ$ are presented here. The computational domain of $-20C < x < 20C$ and $-20C < y < 20C$ is made with a uniform mesh of $-4C < x < 4C$ and $-4C < y < 4C$ near the body to capture the vortices accurately. The domain is discretized into uniform hexagonal cells with further refinement near

the body. The smallest cell size of $0.0125C$ and a time step of $T_f/5000$ are used. The ratio of the smallest cell size to the distance between the Lagrangian nodes is approximately 1. This indicates that one Lagrangian node per cell is used to accurately capture the boundary, at the same time eliminating the need for increasing the number of nodes. The time traces of the horizontal and vertical force coefficients are shown in Fig. 2. The results agree well with that of the literature. This case is used as the base case to find a suitable domain, grid and time step. The vertical force coefficient C_V is used as a standard of comparison for the cases.

Firstly, the domain independence study is conducted on a mesh with the smallest cell size of $0.025C$. The three domains and \bar{C}_V are given in the Table 1. It shows that even though the domain 1 is quite small, it predicts the flow with sufficient accuracy. Further, the instantaneous force in Fig. 3a shows that the domain 1 varies slightly near the peaks. Hence the domain 2 is chosen so that there is a negligible effect of farfield on vortex structures.

In the chosen domain, the grid independence study is done. Three employed grid sizes represent the smallest size of the cell used with equal sizing in x- and y-directions. The sizes and the \bar{C}_V values are given in the Table 2. The coarsest grid has a 2% difference in average value with the intermediate grid but has small oscillations as seen in Fig. 3b. Hence, grid 2 is chosen for reduced oscillations in the moving average.

Domain 2 and grid 2 is used to carry out the time independence study for three time-steps. In all, the CFL number is less than 1 for numerical stability. The time step details and \bar{C}_V values are tabulated in Table 3. From Fig. 4, the time step of $T_f/5000$ is chosen to accurately capture the physics, simultaneously, making the simulations computationally less expensive. In conclusion, the domain 2, grid 2, and a time step of $T_f/5000$ are used for the remainder of the studies.

4. Results and discussion

The results are discussed in two sub-sections, viz. firstly, the effect of stroke plane angle on the vertical forces and the lift enhancement mechanisms; secondly, the role of the dipole jet in the inclined stroke plane kinematics.

4.1 The effect of stroke plane angles on inclined stroke plane hovering

Instantaneous forces:

The evolution of C_V for different stroke plane angles is given in Fig. 4. The downstroke is responsible for most of the vertical force while the upstroke predominantly contributes to the thrust. The unsteady vertical force of the flapping wing and the associated lift enhancement mechanisms are investigated for different stroke plane angles.

On a closer look at the Fig. 4, it can be approximated as having two force peaks for each β during the downstroke. The peaks are defined at points A (which is taken at the instant $t/T_f = 0$) and B (which is taken at the instant $t/T_f = 0.26$) for $\beta=30^\circ$. At 45° , the peaks are at instants $t/T_f = 0.08$ and $t/T_f = 0.3$ marked as points C and D. For $\beta=60^\circ$ first peak is at $t/T_f = 0.1$ which is marked as the point E and the second peak can be approximated at the instant $t/T_f = 0.265$ named point F. For $\beta=75^\circ$, there is a merged single peak at the instant $t/T_f = 0.15$ called point G.

The vorticity contours superimposed with velocity vectors and the pressure contours in Fig. 5 are taken at the first peak (points. A, C, E, G). Similar contours are taken at the instant of the second peak and are given in Fig. 6. At $\beta=30^\circ$, the occurrence of the first peak can be attributed to rotational forces. The peak is low and decreases with the start of the downstroke and wake capture is dominant here. The induced velocity of the counter-rotating vortex pair generated is parallel to the wing and below it (Fig.5a). The white arrow in Fig. 5a represents the wake capture of the second type as it reduces the

vertical forces during the beginning of the downstroke from $t/T_f = 0$ to $t/T_f = 0.1$. The second peak (point B) is caused by the delayed stall in which attached LEV causes high suction on top of the wing (see Fig.6a). Further, this is supported by the added mass (high pressure region at the bottom). The delayed stall is causing this peak and is the main contributor to the high C_V at this stroke plane angle.

For $\beta=45^\circ$, the wake capture acts favourably increasing the C_V and shown as a white arrow in Fig 5b. This causes a high-pressure region underneath the wing which is seen as the red region in the pressure contour. Analogous to the $\beta=30^\circ$, the delayed stall is causing the second peak (point D), although added mass also contributes to part of the high lift (see Fig. 6b).

At $\beta=60^\circ$, the wake capture partly contributes to increases in C_V initially in the same way as $\beta=45^\circ$ (Fig. 5c), but the favourable pressure distribution contributes to the peak. It can be understood from the high-pressure present underneath the wing along with low pressure on top surface of the wing. Thus the the growing LEV on top of the wing with the wake capture at the bottom is able to explain high vertical force. The second peak or point D is more of a flat region of the constant C_V which is sustained by the delayed stall and added mass (Fig. 6c).

At $\beta=75^\circ$, added mass and the delayed stall causes favourable pressure gradients, contributing to the high C_V of the merged peak. The single is peak is shown in both the Figs.5d and 6d. The LEV and TEV becomes detached as the wing moves down and hence, there is no second peak.

At $\beta=30^\circ$, the high vertical force is caused by the delayed stall in the second half of the downstroke and the lower force is caused by the wake capture in the first half. At $\beta=45^\circ$, the first peak predominantly contributes to the vertical force is supported by both the wake capture and added mass while the second peak is caused by the delayed stall and added mass. For $\beta=60^\circ$, the first peak is the main region of force enhancement where the wake capture and the delayed stall acts. Point D is in a region, where the de-

layed stall and added mass maintains the vertical force. At $\beta=75^\circ$, added mass and the delayed stall together contributes to most of the C_V in the first half and then force drops.

On the whole, the class of flows with varying stroke plane angles has contributions from wake capture, added mass and delayed stall to a high C_V . As the 2D kinematics taken for the study has synchronous translation and rotation, it poses difficulties in the extrication of force enhancements. Nevertheless, the study of the peaks reveals a few common characteristics. At $\beta=30^\circ$, which represents a small inclined stroke plane angle is producing vertical forces in the second force peak (the second half of the downstroke), whereas $\beta=75^\circ$ (which stands for the high stroke plane angle) is producing a high C_V in the first half of the downstroke. In the intermediate range of β , the force trace can have two peaks or two locations contributing significantly to lift. The first peak is dominated by the wake capture whereas the second peak is dominated by the delayed stall.

Another interesting flow feature is the presence of dipole and its movement with varying stroke plane angles. The dipole is further analysed, as described in section 4.2 to identify flow patterns and its influence on the vertical forces.

Average forces and the dominant lift enhancement mechanisms:

The table 4 indicates that the \bar{C}_V increases with the stroke plane angle up to 60° and then decreases. This is in line with the observation of dragonflies whose stroke plane angle is around 60° during hover. Here, we are able to explain it from the vortex dynamics. The wake capture, added mass and the delayed stall can explain the instantaneous vertical force variation in a cycle. From the instantaneous forces, it can be observed that the interplay between the wake capture, added mass and the delayed stall contributes to the vertical forces. These mechanisms alter the instantaneous C_V peaks with stroke plane

angle. However, the overall outcome is that the average vertical force is the best possible at $\beta=60^\circ$. This is due to the arrangement of the lift enhancement mechanism which results in high vertical forces.

4.2 Dipole Jet

In this article, Dipole jet is defined as the induced jet of air between vortex pair shed in the current flapping cycle. Unlike induced velocity due to wake capture defined near the body, velocity of the dipole jet defined here, will be a part of the dipole shed during the current cycle. This dipole carries the momentum away from the wing giving an opposite force on the wing. A vortex pair is formed in every cycle and vortex street pattern appears near the wing with continuous flapping. After the simulation reaches a periodic stage, the dipole jet is studied to understand and classify the flow pattern when the stroke plane angles are varied.

The dipole jet properties are taken at vertical force peaks used in the previous sections. The vertical force peaks are chosen for the analysis as they are the major contributors of the \bar{C}_V . To visualize the jets, the instantaneous velocity contours during the first peak (points A, C, E and G) are presented in Fig. 7 for each stroke plane angle. Red region represents the ‘dipole jet’ moving away from the body for each angle. The velocity is high for the first vortex pair and reduces significantly for the next ones. For $\beta=30^\circ$, the jet is very close to the wing and moves towards its right. For the other stroke plane angles, the dipole jets move downward (Figs. 7b, 7c and 7d).

To quantify the velocities, a line is drawn between the vortex centroids and velocities are plotted over the centreline. Vortex centroids are calculated^[36] from their respective vorticity contour. V_D is the jet velocity and s is taken as the distance between the centroids of the two vortices CV (Clockwise Vortex) and CCV (Counter-Clockwise Vortex). Fig. 8 is a schematic diagram showing the vortex pairs during the first force peak (solid line) and the second force peak (dotted line). The first peaks refer to

points A, C, E and G and second peaks refer to B, D, F and G for the stroke plane angles $\beta=30^\circ, 45^\circ, 60^\circ, 75^\circ$ as used in the previous section. Four characteristics namely, the maximum vertical velocity magnitude, the inclination with respect to the horizontal, the spread of the velocity profile and the location of the dipole are carefully studied at the two peaks for different stroke plane angles.

Vertical velocity magnitude and the inclination

Table 5 gives the maximum vertical velocity and inclinations of the dipole jet at both the peaks. From $\beta=30^\circ$ to $\beta=60^\circ$, the maximum vertical velocity increases and then decreases for $\beta=75^\circ$. This trend is followed by both the peaks. The main difference is the reduced vertical velocities for the second peak compared to the first peak. For $\beta=30^\circ$, the jet is sideways and hence the vertical component of velocity is very low. For $\beta=45^\circ$ and 60° , the jet is downward and produces significant vertical velocity. For $\beta=75^\circ$, the jet inclination is reduced showing a small reduction in vertical velocity. In addition, it is essential to note that the magnitude of vertical velocities are comparable to U except for $\beta=30^\circ$. The angles are measured at both the peaks and are represented by γ_1 and γ_2 respectively. For $\beta=30^\circ$, the jet is inclined at around 20° for both the peaks. For $\beta=45^\circ$ and 60° , the velocity is inclined around 80° and $\beta=75^\circ$, it is around 60° . This observation is showing similar trend as the maximum vertical velocity.

The spread of the velocity profile

Fig. 9 shows the vertical velocity profile V_D plotted during the first and second force peaks for each stroke plane angle. It shows that the spread of the velocity profile. It is clear that at $\beta=30^\circ$, the dipole is deflected sideways and for the rest of the stroke plane angles, it is downward. This might indicate a cut-off between $\beta=30^\circ$ and 45° beyond which the dipole jet is vertical. But the rest of the angles show a clear trend of the narrowing jet with β . This trend remains the same for both the peaks. As the angles increase the dipoles are aligned closer to each other and the jet becomes narrow.

From the characteristics of the dipole jet discussed above, the overall trend of the increasing dipole jet velocity till $\beta=60^\circ$ can be attributed to the downward movement of the dipoles and the narrower jet. For $\beta=75^\circ$, the vertical velocity reduces as the inclination decreases. In all, $\beta=60^\circ$ shows a high vertical velocity. As momentum carried by the dipole reflects on the force generated, the properties of the dipole can be used to find the trend of \bar{C}_V . Moreover, it can be observed that the analysis carried out in second force peaks shows a similar trend as the first peak but with a lower magnitude of the vertical velocities. Hence, analysis in one peak could sufficiently describe the variation in \bar{C}_V .

Location of the dipole

The location of the dipole is of significance as it describes an approximate region of influence of the flapping wing. The co-ordinates of the centroid of the dipole vortices during the two force peaks are plotted in Fig.11. The vertical position of the dipole shifts down with increase in stroke plane angle. It shows that the vortex cores of the dipole moves a maximum distance of $3.86C$ downward and $2.08C$ sideways for the stroke plane angles investigated. As seen in the previous section, the vertical velocity of dipole jet is comparable to U and anything that affects the dipole will modify the vertical force. This could be interpreted in two ways. Any object placed in the region of the dipole whether it is a wing or a wall, it will significantly alter the \bar{C}_V . Also, any object which generates vortex structures that disturbs the centroids could result in change in \bar{C}_V . In other words, by knowing the location of the dipole for each stroke plane angle, the minimum distance at which another body can be placed without causing any change in forces can be arrived at.

The wake analysis carried out in this section indicates that the maximum dipole jet and its features (magnitude, inclination, spread and its location) are shown to significantly change with stroke plane

angle. Together, they are a good pointer to the variation of \bar{C}_V with β . It shows that mid-range of stroke plane angle is favourable for high downward jet which in turn contributes to high vertical forces.

By knowing the location of the dipole for each stroke plane angle, the minimum distance at which another body can be placed without causing any change in forces can be arrived at. In other words, one might find a significant change in the peaks, when another body or wall, affects the dipole when placed within the region. Further studies on multibody dynamics could reveal more information on the same. Since its magnitude is representative of the \bar{C}_V any change in the dipole jet magnitude could result in the change in the optimum stroke plane angle

5 Conclusion

The studies on the inclined stroke plane kinematics are carried out successfully along with the wake analysis of the dipole jet. It revealed a few key points. The vertical force and the vortex dynamics has shown that lift enhancement mechanisms such as added mass, the wake capture and delayed stall explains the variation of the vertical forces when the stroke plane angles are varied. A dipole with an induced jet is produced for every cycle and its properties change with the stroke plane angle. As the vertical velocity of the dipole jet increases, vertical force acting on the wing increases due to momentum transfer. The location of the dipole, maximum jet speed and its inclination can be used to assess the change in vertical force production. From this study, it is clear that the study of dipole jet could explain the \bar{C}_V patterns. It provides an alternate approach to explain the changes in \bar{C}_V in a given class of flapping wing kinematics. The location of the dipole is found to be crucial for the study of multiple flapping wings or insects or wall effects. An important result from the study is that the analysis of the lift enhancement mechanism as well as the dipole jet was able to explain the high vertical force produced by the stroke plane angle of 60° in hover.

References

- [1] Ellington C P. The Aerodynamics of Hovering Insect Flight. I . The Quasi-Steady Analysis. *Philosophical Transactions of the Royal Society of London Series B, Biological Sciences*, 1984,**305**,1-15.
- [2] Sane S P. The aerodynamics of insect flight. *The Journal of Experimental Biology*, 2003,**206**,4191-4208.
- [3] Lehmann F O. The mechanisms of lift enhancement in insect flight. *Naturwissenschaften*, 2004,**91**,101-122.
- [4] Dickinson M H, Götz K G. Unsteady aerodynamic performance of model wings at low Reynolds numbers. *Journal of Experimental Biology*, 1993,**174**,45-64.
- [5] Dickinson M H, Lehmann F O, Sane S P. Wing rotation and the aerodynamic basis of insect flight. *Science*, 1999,**284**,1954-1960.
- [6] Lua K B, Lim T T, Yeo K S. Effect of wing-wake interaction on aerodynamic force generation on a 2D flapping wing. *Experiments in Fluids*, 2011,**51**,177-195.
- [7] Sane S P, Dickinson M H. The aerodynamic effects of wing rotation and a revised quasi-steady model of flapping flight. *The Journal of Experimental Biology*, 2002,**205**,1087-1096.
- [8] Sane S P, Dickinson M H. The control of flight force by a flapping wing: lift and drag production. *The Journal of Experimental Biology*, 2001,**204**,2607-2626.
- [9] Jane Wang Z. Two Dimensional Mechanism for Insect Hovering. *Physical Review Letters*, 2000,**85**,2216-2219.
- [10] Sudhakar Y, Vengadesan S. Flight force production by flapping insect wings in inclined stroke plane kinematics. *Computers and Fluids*, 2010,**39**,683-695.
- [11] Meng X, Liu Y, Sun M. Aerodynamics of Ascending Flight in Fruit Flies. *Journal of Bionic Engineering*, 2017,**14**,75-87.
- [12] Meng X, Sun M. Wing Kinematics, Aerodynamic Forces and Vortex-wake Structures in Fruit-flies in Forward Flight. *Journal of Bionic Engineering*, 2016,**13**,478-490.
- [13] Wu J H. Unsteady aerodynamic forces of a flapping wing. *Journal of Experimental Biology*, 2004,**207**,1137-1150.
- [14] Ellington C P, Vandenberg C, Willmott A P, Thomas A L. Leading-edge vortices in insect flight. *Nature*, 1996.
- [15] Wang Z J, Birch J M, Dickinson M H. Unsteady forces and flows in low Reynolds number hovering flight: two-dimensional computations vs robotic wing experiments. *The Journal of Experimental Biology*, 2004,**207**,449-460.
- [16] Gao T, Lu X Y. Insect normal hovering flight in ground effect. *Physics of Fluids*, 2008,**20**,087101.

-
- [17] Maeda M, Liu H. Ground effect in fruit fly hovering: A three-dimensional computational study. *Journal of Biomechanical Science and Engineering*, 2013,**8**,344-355.
- [18] Kolomenskiy D, Maeda M, Engels T, Liu H, Schneider K, Nave J C. Aerodynamic ground effect in fruitfly sized insect takeoff. *PLoS ONE*, 2016,**11**.
- [19] Srinidhi N G, Vengadesan S. Ground effect on tandem flapping wings hovering. *Computers and Fluids*, 2017,**152**,40-56.
- [20] Viswanath K, Tafti D K. Effect of Frontal Gusts on Forward Flapping Flight. *AIAA Journal*, 2010,**48**,2049-2062.
- [21] De M M, Mathur J S, Vengadesan S. Recurrence studies of insect-sized flapping wings in inclined-stroke plane under gusty conditions. *Sādhanā*, 2019,**44**,67.
- [22] Xie C M, Huang W X. Vortex interactions between forewing and hindwing of dragonfly in hovering flight. *Theoretical and Applied Mechanics Letters*, 2015,**5**,24-29.
- [23] Lua K B, Lu H, Zhang X H, Lim T T, Yeo K S. Aerodynamics of two-dimensional flapping wings in tandem configuration. *Physics of Fluids*, 2016,**28**,121901.
- [24] Gadde S N, Vengadesan S. Lagrangian Coherent Structures in Tandem Flapping Wing Hovering. *Journal of Bionic Engineering*, 2017,**14**,307-316.
- [25] Weis-fogh T. Quick estimates of flight fitness in hovering animals, including novel mechanisms for lift production. *Journal of Experimental Biology*, 1973,**59**,169-230.
- [26] Ellington C P. The Aerodynamics of Hovering Insect Flight. III. Kinematics. *Philosophical Transactions of the Royal Society B: Biological Sciences*, 1984,**305**,41-78.
- [27] Wang Z J. The role of drag in insect hovering. *Journal of Experimental Biology*, 2004,**207**,4147-4155.
- [28] Trizila P, C-K K, Anono H, W S, Visbal M. Low-Reynolds-Number Aerodynamics of a Flapping Rigid Flat Plate. *AIAA Journal*, 2011,**49**,806-823.
- [29] Jasak H, Tuković Ž. Immersed Boundary Method in FOAM:Theory, Implementation and Use. http://www.tfd.chalmers.se/~hani/kurser/OS_CFD_2015/HrvojeJasak/ImmersedBoundary.pdf. Published 2015.
- [30] foam-extend-4.0.
- [31] Weller H G, Tabor G, Jasak H, Fureby C. A tensorial approach to computational continuum mechanics using object-oriented techniques. *Computers in Physics*, 1998,**12**,620.
- [32] Charles S. Peskin. Flow patterns around heart valves: A numerical method. *Journal of Computational Physics*, 1972,**10**,252-271.
- [33] Singh K M, Nonaka N, Oh U. Immersed Boundary Method for cfd Analysis of Moving Boundary. In: *ASME 2015 International Mechanical Engineering Congress and Exposition*. Houston,Texas; 2015:1-10.
- [34] Senturk U, Brunner D, Herzog N, Jasak H, Rowley C W, Smits A J. Benchmark Simulations of

Flow Past Moving Rigid Bodies Using a Sharp Interface Immersed Boundary Method. In: *Ninth International Conference on Computational Fluid Dynamics (ICCFD9)*. Istanbul, Turkey; 2016:1-8.

- [35] Xu S, Wang Z J. An immersed interface method for simulating the interaction of a fluid with moving boundaries. *Journal of Computational Physics*, 2006,**216**,454-493.
- [36] Leweke T, Le Dizès S, Williamson C H K. Dynamics and Instabilities of Vortex Pairs. *Annual Review of Fluid Mechanics*, 2016,**48**,507-541.

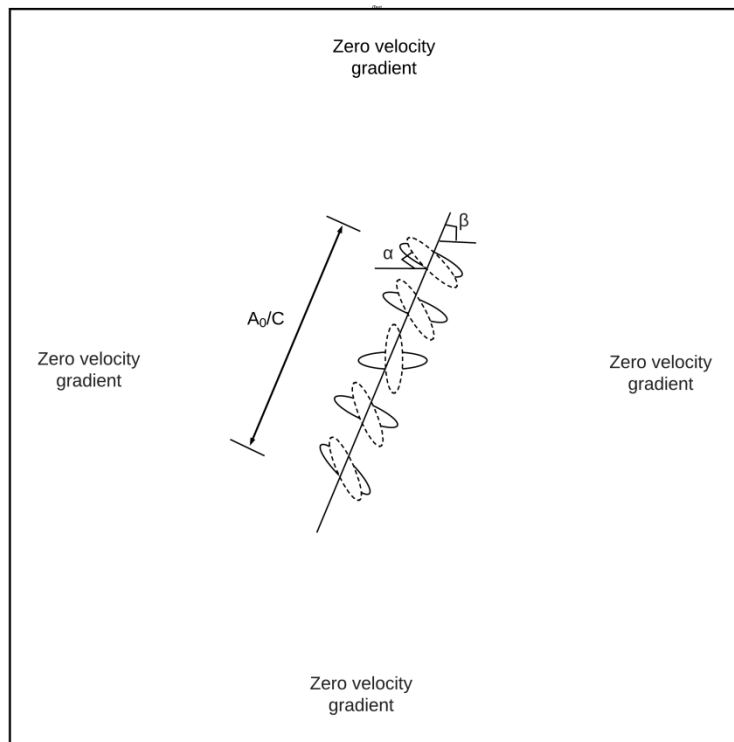
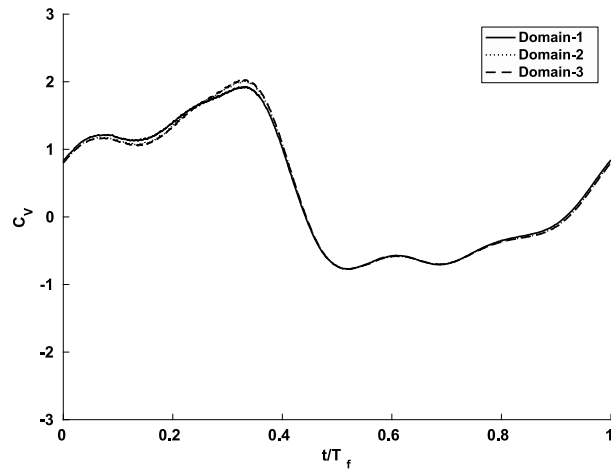
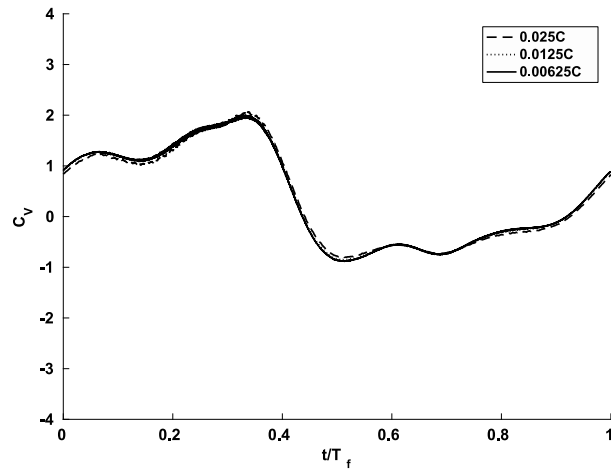


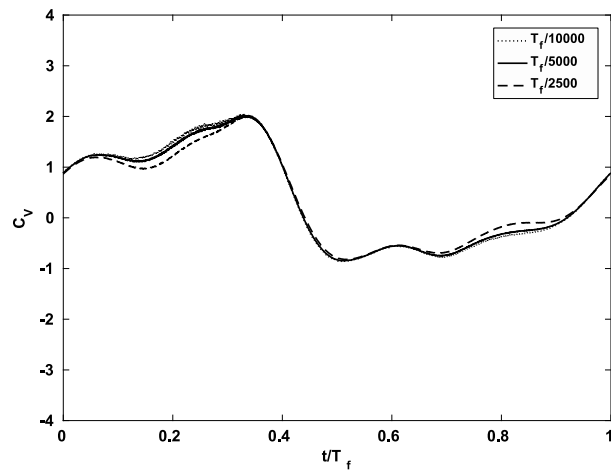
Fig. 1 Schematic diagram showing the kinematics, domain and boundary conditions of the current study. The solid line indicates the downstroke and the dotted line indicates the upstroke



(a)



(b)



(c)

Fig. 2 C_v vs. cycle time for (a) Domain independence study (b) Grid independence study (c) Time independence study

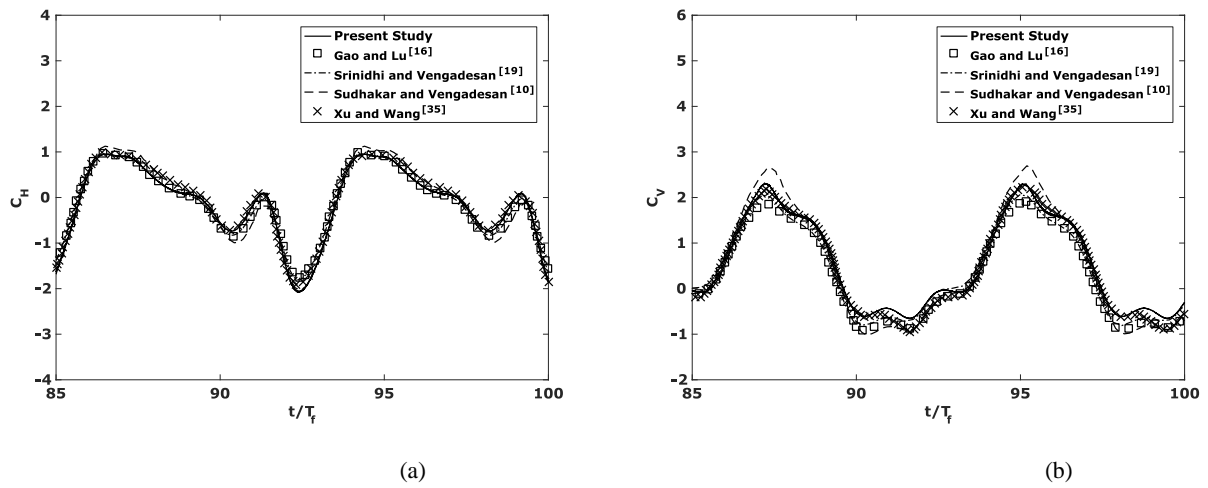


Fig. 3 Force trace for dragonfly kinematics (a) horizontal force coefficient (b) vertical force coefficient

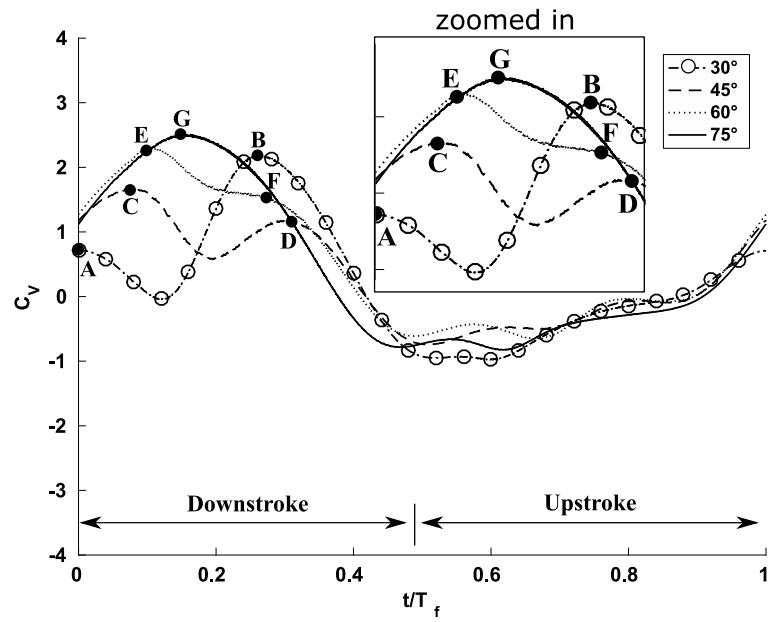


Fig. 4 Vertical force coefficient history for one cycle for different stroke plane angle

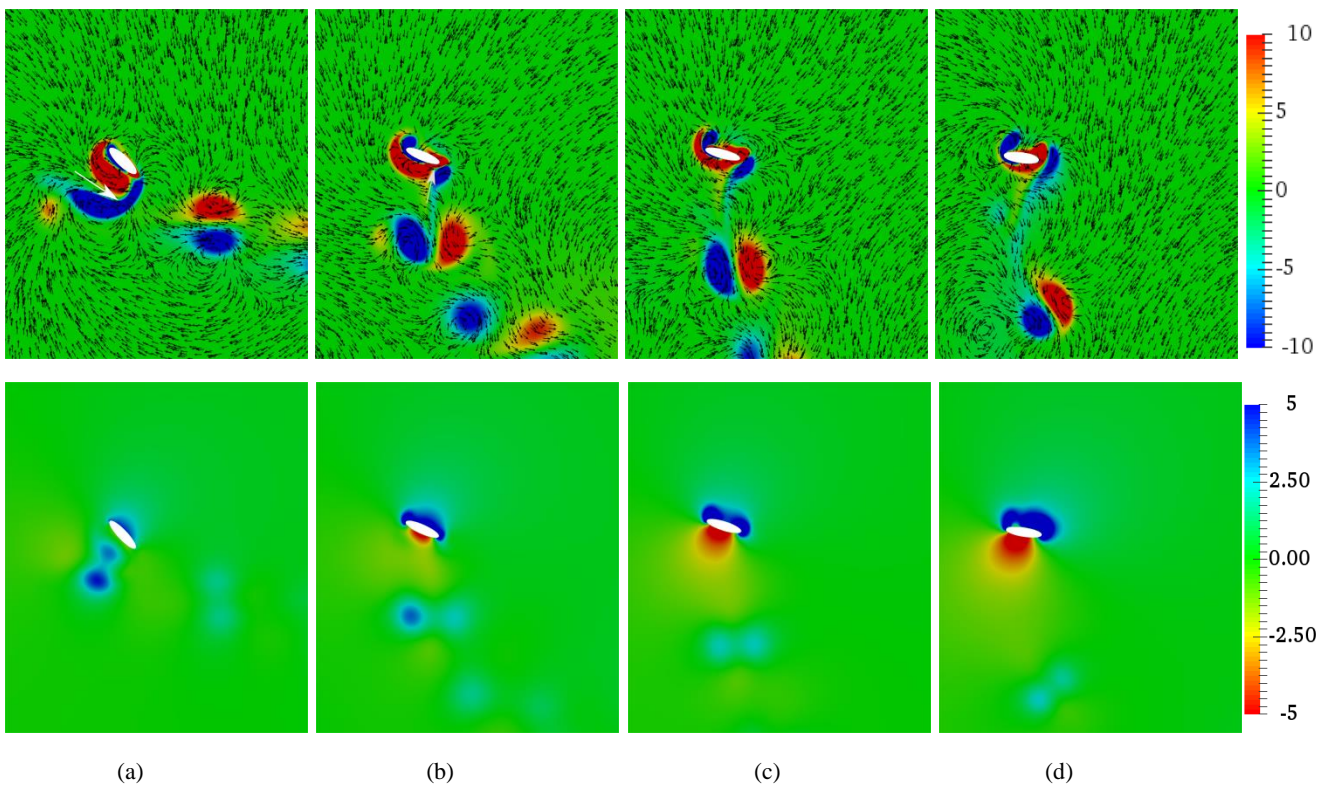


Fig. 5 Vorticity with velocity vector and pressure contour during for the first vertical force peak for stroke plane angles (a) 30° (b) 45° (c) 60° (d) 75°. Vorticity is measured in s^{-1} and the pressure is measure with respect to atmospheric pressure in pa .

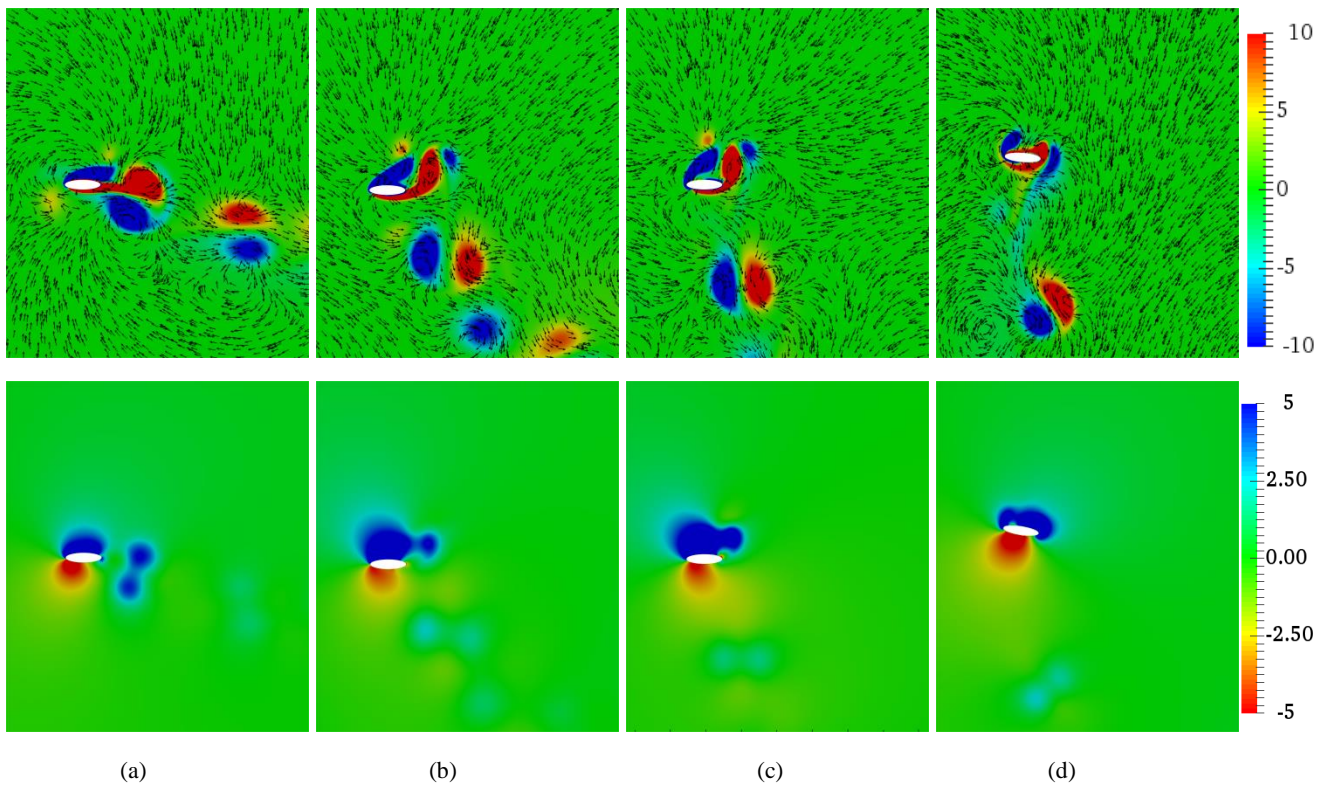


Fig. 6 Vorticity with velocity vector and pressure contour during for the second vertical force peak for stroke plane angles (a) 30° (b) 45° (c) 60° (d) 75°. Vorticity is measured in s^{-1} and the pressure is measure with respect to atmospheric pressure in pa .

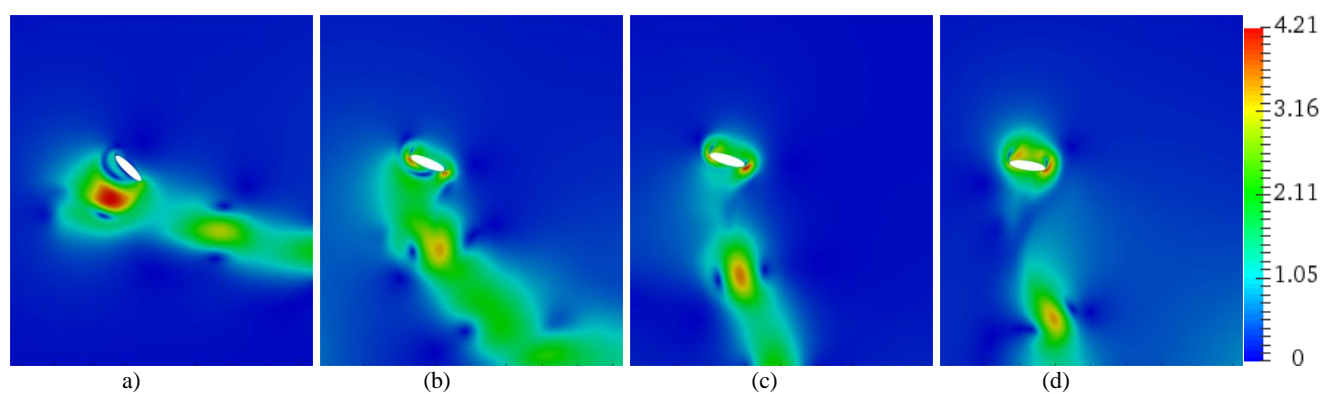


Fig. 7 Velocity contour showing the dipole jet (red region) taken at the first peak for stroke plane angles (a) 30° (b) 45° (c) 60° (d) 75°. Velocity is measured in *m/s*

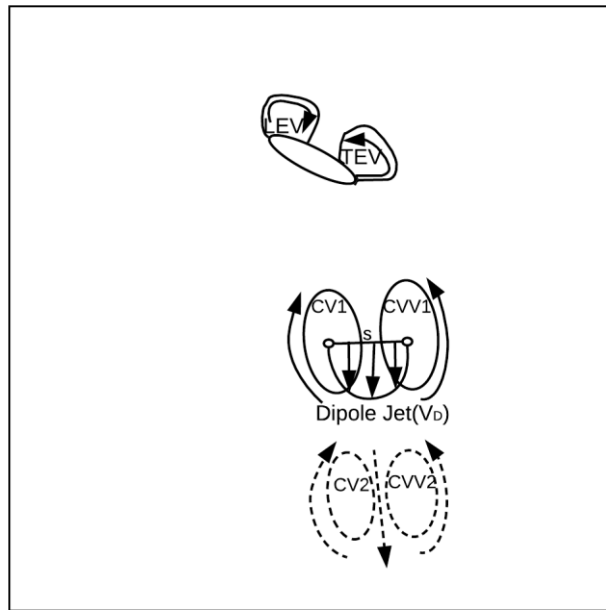


Fig. 8 The schematic diagram shows the dipole generated and the jet profile taken on the centreline. The dipole is represented by the solid line taken during the first peak. The dipole represented by the dotted line is taken during the second peak.

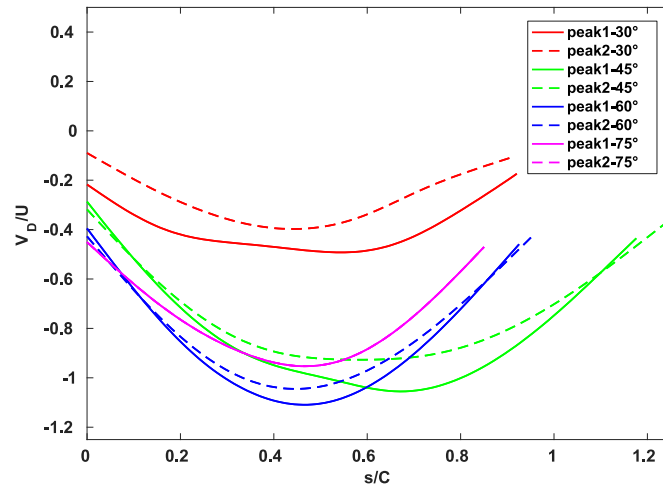


Fig. 9 The velocity profile on the centreline joining the centroid of the dipole for the first peaks (solid line) and second peaks (dotted line)

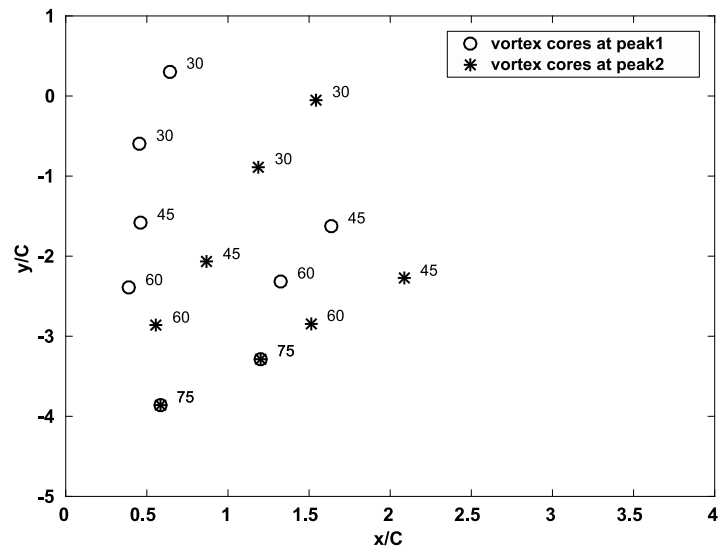


Fig. 10 Location of the centroids of the dipole cores with changing stroke plane angles in degrees.

Table 1 Domain independence study

Domain	Size	\bar{C}_V
1	$10C < x < 10C, 2C < y < 10C$	0.3833
2	$-20C < x < 20C, 2C < y < 20C$	0.3768
3	$-30C < x < 30C, 2C < y < 30C$	0.3755

Table 2 Grid independence study

Grid	Size	\bar{C}_V
1	0.025C	0.3721
2	0.0125C	0.3810
3	0.00625C	0.3854

Table 3 Time independence study

Case	Time step	\bar{C}_v
1	Tf/2500	0.3844
2	Tf/5000	0.3927
3	Tf/10000	0.3992

Table 4 Cycle average vertical forces for different stroke plane angles

Case	β	\bar{C}_v
1	30°	0.2080
2	45°	0.3070
3	60°	0.5110
4	75°	0.4348

Table 5 Maximum vertical velocity and the inclination angle for different stroke plane angle

β	$V_{y_{max1}}(\text{m/s})$	$V_{y_{max2}}(\text{m/s})$	γ_1	γ_2
30°	-1.55	-1.25	22.4°	17.3°
45°	-3.32	-2.9	79.5°	79.5°
60°	-3.49	-3.28	78.6°	79.8°
75°	-2.99	-2.99	61.5°	61.5°

Fig. 1 Schematic diagram showing the kinematics, domain and boundary conditions of the current study. The solid line indicates the downstroke and the dotted line indicates the upstroke	17
Fig. 2 C_v vs. cycle time for (a) Domain independence study (b) Grid independence study (c) Time independence study	18
Fig. 3 Force trace for dragonfly kinematics (a) horizontal force coefficient (b) vertical force coefficient	19
Fig. 4 Vertical force coefficient history for one cycle for different stroke plane angle	20
Fig. 5 Vorticity with velocity vector and pressure contour during for the first vertical force peak for stroke plane angles (a) 30° (b) 45° (c) 60° (d) 75°. Vorticity is measured in s^{-1} and the pressure is measure with respect to atmospheric pressure in pa	21
Fig. 6 Vorticity with velocity vector and pressure contour during for the second vertical force peak for stroke plane angles (a) 30° (b) 45° (c) 60° (d) 75°. Vorticity is measured in s^{-1} and the pressure is measure with respect to atmospheric pressure in pa	22
Fig. 7 Velocity contour showing the dipole jet (red region) taken at the first peak for stroke plane angles (a) 30° (b) 45° (c) 60° (d) 75°. Velocity is measured in m/s	23
Fig. 8 The schematic diagram shows the dipole generated and the jet profile taken on the centreline. The dipole is represented by the solid line taken during the first peak. The dipole represented by the dotted line is taken during the second peak.	24
Fig. 9 The velocity profile on the centreline joining the centroid of the dipole for the first peaks (solid line) and second peaks (dotted line)	25
Fig. 10 Location of the centroids of the dipole cores with changing stroke plane angles in degrees.....	26
Table 1 Domain independence study	27
Table 2 Grid independence study	28
Table 3 Time independence study	29
Table 4 Cycle average vertical forces for different stroke plane angles.....	30
Table 5 Maximum vertical velocity and the inclination angle for different stroke plane angles.....	31